Journal of
Micro/Nanolithography,
MEMS, and MOEMS

Nanolithography.SPIEDigitalLibrary.org

# Fabrication and characterization of microstructures created in thermally deposited arsenic trisulfide by multiphoton lithography

Casey M. Schwarz
Chris N. Grabill
Gerald D. Richardson
Sherya Labh
Anna M. Lewis
Aadit Vyas
Benn Gleason
Clara Rivero-Baleine
Kathleen A. Richardson
Alexej Pogrebnyakov
Theresa S. Mayer
Stephen M. Kuebler

Casey M. Schwarz, Chris N. Grabill, Gerald D. Richardson, Sherya Labh, Anna M. Lewis, Aadit Vyas, Benn Gleason, Clara Rivero-Baleine, Kathleen A. Richardson, Alexej Pogrebnyakov, Theresa S. Mayer, Stephen M. Kuebler, "Fabrication and characterization of microstructures created in thermally deposited arsenic trisulfide by multiphoton lithography," *J. Micro/Nanolith. MEMS MOEMS* **16**(2), 023508 (2017), doi: 10.1117/1.JMM.16.2.023508.

# Fabrication and characterization of microstructures created in thermally deposited arsenic trisulfide by multiphoton lithography

**Casey M. Schwarz,[a] Chris N. Grabill,[a] Gerald D. Richardson,[a] Sherya Labh,[a] Anna M. Lewis,[a] Aadit Vyas,[a] Benn Gleason,[b,c] Clara Rivero-Baleine,[d] Kathleen A. Richardson,[b] Alexej Pogrebnyakov,[e] Theresa S. Mayer,[e] and Stephen M. Kuebler[a,b,f,*]**
[a]University of Central Florida, Department of Chemistry, Orlando, Florida, United States
[b]University of Central Florida, CREOL, The College of Optics and Photonics, Orlando, Florida, United States
[c]University of Clemson, Materials Science and Engineering Department, Clemson, South Carolina, United States
[d]Lockheed Martin, Orlando, Florida, United States
[e]Pennsylvania State University, Department of Electrical Engineering, University Park, Pennsylvania, United States
[f]University of Central Florida, Physics Department, Orlando, Florida, United States

**Abstract.** A detailed study of multiphoton lithography (MPL) in arsenic trisulfide ($As_2S_3$) films and the effects on nanoscale morphology, chemical networking, and the appearance of the resulting features by the chemical composition, deposition rate, etch processing, and inclusion of an antireflection (AR) layer of $As_2Se_3$ between the substrate and the $As_2S_3$ layer is reported. MPL was used to photo-pattern nanostructured arrays in single- and multilayer films. The variation in chemical composition for laser-exposed, UV-exposed, and unexposed films is correlated with the etch response, nanostructure formation, and deposition conditions. Reflection of the focused beam at the substrate back into the film produces standing wave interference that modulates the exposure with distance from the substrate and produces nanobead structures. The interference and the modulation can be controlled by the addition of an AR layer of $As_2Se_3$ deposited between the substrate and the $As_2S_3$ film. Relative to structures produced in a single-layer $As_2S_3$ film having no AR layer, photo-patterning in the multilayer $As_2S_3$-on-$As_2Se_3$ film yields pillar-shaped structures that are closer to the targeted shape and are narrower (120 versus 320 nm), more uniform, and better adhering to the substrate. Processing methods are demonstrated for fabricating large-area arrays with diffractive optical function. 
[DOI: 10.1117/1.JMM.16.2.023508]

Keywords: chalcogenide glass; arsenic trisulfide; arsenic triselenide; multiphoton lithography; direct laser writing; microfabrication.

Paper 17020 received Mar. 3, 2017; accepted for publication May 26, 2017; published online Jun. 19, 2017.

## 1 Introduction

There is growing interest in the development of optics that function at wavelengths in the infrared (IR) for applications in diagnostic medicine, environmental sensing, space exploration, and search-and-rescue tools.[1,2] To achieve many of these applications, it is important to produce light-weight, low-profile, robust optics with good thermal properties and to reduce manufacturing cost and time. Most bulk, IR optics are made of Si, Ge, or ZnSe crystalline materials, which are costly, heavy, and sometimes difficult to manufacture.[3–5] Widely used optical fabrication techniques, such as computer numerical control processing and diamond turning, can be costly due to material-specific processing methodologies, whereas less expensive alternatives, such as precision glass molding, cannot be extended to crystalline components. Single-material IR components are dense and heavy, and often have limited optical function.[6] These factors often hinder high-volume commercial production of multielement IR optical systems. Hence, there is a pressing need for new IR materials that offer improved optical, mechanical, and thermal performance with a smaller footprint.

Chalcogenide glasses (ChGs) have emerged as promising candidates for IR applications due to their excellent IR transparency, large index of refraction, modest coefficients of thermal expansion (CTE), tailorable thermo-optic coefficient ($dn/dT$), and unique optical functionality over a range of form factors and environmental conditions.[7] IR glasses have high refractive indices ($n \sim 2$ to 3), so IR-glass optics must be coated with an antireflection (AR) layer. Low CTE is particularly important for applications in which the operating temperature can vary widely,[8] and a large mismatch in the CTE can cause AR layers to delaminate, leading to damage or device failure, and it can introduce strain between components that alters the polarization of light.[9–11] ChGs are multicomponent amorphous materials that can be formed as bulk, thin-film, or fiber components and can be processed into functional optics more quickly and at a lower cost than single-component crystalline materials.

Bulk ChG blanks or lenses can be further modified using molding or diamond turning to create kinoform structures on the surface that modify the reflectivity.[5,12,13] Similar efforts have been made to a lesser extent on homogeneous films where surface roughness is minimized to reduce scatter loss, either through precise deposition protocols or postprocessing (i.e., thermal reflow).[14] This has been extensively investigated in the use of ChG films, waveguides, and resonators in planar photonics structures;[15,16] the composition of the ChG is tailored to small-footprint structures with high index

*Address all correspondence to: Stephen M. Kuebler, E-mail: kuebler@ucf.edu

1932-5150/2017/$25.00 © 2017 SPIE

contrast that are suitable for on-chip integration with dissimilar materials (i.e., Si, PbTe, and polymers). Most of these uses have been explored in homogeneous-bulk or thin-film glass components without additional surface structuring to further extend their optical functionality. The present work is motivated in part by the need to explore material systems and processes that can be used to create optically functional surfaces and three-dimensional (3-D) structures that augment the performance of IR optics and optical systems.

Arsenic trisulfide ($As_2S_3$) glass has been extensively studied as it offers potential for IR applications due to its optical bandgap of $E_g = 2.35$ eV ($\lambda \approx 517$ nm), high transparency from 620 nm to 11 $\mu$m, an intermediate refractive index of $n = 2.45$ to 2.53, and photosensitivity that can be used to create functional structures and devices.[17,18] Thermal deposition of bulk $As_2S_3$ fragments the network solid, creating molecular clusters—such as $As_4S_6$, $As_4S_4$, and $S_8$—that can be deposited as photosensitive thin films.[17,19–22] The films can then be photo-patterned through masked- or scanned-laser exposure. Photoexcitation cross-links the material back into a glassy network solid, such as an organic photoresist. Photo-patterned $As_2S_3$ films can then be immersed in a polar solvent to selectively dissolve away unexposed material, revealing the targeted structure.[17,19–21,23–25] Multiphoton lithography (MPL) in thermally deposited $As_2S_3$ films has been used to produce 3-D structures, such as woodpile photonic crystals, nanowires, and waveguides.[17–21,23,24,26,27] These types of structures are useful in electrical and optical applications, such as sensors, waveguides, acousto-optics, detectors, and imaging systems.[1,2,28,29] Film deposition and processing have been found to influence how nanostructures are formed through MPL.[19–21] By investigating how film deposition and processing affect the properties and performance of $As_2S_3$, functional properties, such as index of refraction $n$, can be controlled and optimized for desired applications.

This work reports a detailed study of MPL in thermally deposited $As_2S_3$ films and the effects on the nanostructure morphology, chemical networking, and the appearance of the resulting features by the chemical composition, film deposition rate, etch processing, and the inclusion of an AR layer of $As_2Se_3$ between the substrate and the photo-patternable $As_2S_3$. The variation in chemical structure for laser-exposed, UV-exposed, and unexposed films is correlated with the etch response, nanostructure formation, and deposition conditions for each film. To date, photo-processing in thermally deposited ChG films with an AR layer has not been reported. In films without an AR layer, focused beam reflection at the silicon substrate back into the interaction volume of the material is shown to produce standing wave interference that modulates the film exposure with distance from the substrate and results in the production of nanobead structures. The addition of an AR layer reduces interference and modulation.[14] By exploring the addition of an AR layer and photo-patterning in a multilayer $As_2S_3$-on-$As_2Se_3$ ChG film, processing conditions that enable precise control over structure size and shape for targeted applications are identified.

## 2 Methods

### 2.1 *Thermal Deposition of Films*

The sample films were produced by thermally depositing layers of $As_2S_3$ and $As_2Se_3$ onto polished silicon wafers from bulk ChGs. Spectroscopic ellipsometry showed that a thin $SiO_2$ native oxide layer was present on the surface of all wafers at a thickness of 4 nm. Bulk ChGs were prepared using traditional melt-quench processes described elsewhere.[30] Throughout this paper, films are referred to by both a label and a number (Table 1). The label indicates the film composition and thickness. The number indicates the individual film. All films were transported in petri dishes wrapped with aluminum foil and stored in an amber desiccator in a cupboard to prevent unintended exposure to ambient light and moisture.

**Table 1** Film number, type/composition, rate of $As_2S_3$ deposition, thickness of the $As_2S_3$ layer, and color of the sample. The values listed under "thickness" refer to the $As_2S_3$ layer for all films.

| Film number | Type | Film composition | $As_2S_3$ deposition rate (Å s$^{-1}$) | Thickness (nm) | Color |
|---|---|---|---|---|---|
| 1 | Single layer | $As_2S_3$ | 80 | $164 \pm 3$ | Blue |
| 2 | Single layer | $As_2S_3$ | 80 | $159 \pm 6$ | Blue |
| 3 | Single layer | $As_2S_3$ | 25 | $170 \pm 8$ | Pink |
| 4 | Single layer | $As_2S_3$ | 25 | $166 \pm 3$ | Pink |
| 5 | Single layer | $As_2S_3$ | 25 | $172 \pm 9$ | Pink |
| 6 | Single layer | $As_2S_3$ | 27 | $1075 \pm 0.8$ | Pink |
| 7 | Multilayer | $As_2S_3$-on-$As_2Se_3$ | 30 | $896 \pm 13$ | Green |

Two types of thin films were produced. The first film type was a "single-layer $As_2S_3$ film" (#1 to #6) that consists of a layer of $As_2S_3$ deposited on the substrate. Films (#1 to #6) were deposited using a Kurt Lesker Thermal Evaporation chamber. $As_2S_3$ films #1 and #2 were deposited at a rate of 80 Å s$^{-1}$, were blue in color, and had final thicknesses of 164 nm $\pm$ 3 nm and 159 nm $\pm$ 6 nm, respectively. $As_2S_3$ films #3, #4, and #5 were deposited at a rate of 25 Å s$^{-1}$, were pink, and had final thicknesses of 170 nm $\pm$ 8 nm, 166 nm $\pm$ 3 nm, and 172 nm $\pm$ 9 nm, respectively. $As_2S_3$ film #6 was deposited at a rate of 27 Å s$^{-1}$, was pink, and had a thickness of 1075 nm $\pm$ 0.8 nm.

The second film type was a "multilayer $As_2S_3$-on-$As_2Se_3$ film" (#7) that consists of an AR layer of $As_2Se_3$ deposited on the silicon substrate followed by a layer of $As_2S_3$. Film #7 was prepared using a Kurt Lesker Thermal Multisource Evaporator deposition chamber. The $As_2Se_3$ layer was thermally deposited at a rate of 4 Å s$^{-1}$ and had a final thickness of 203 nm $\pm$ 3 nm. The $As_2S_3$ layer was thermally deposited at a rate of 30 Å s$^{-1}$ and had a final thickness of 896 nm $\pm$ 13 nm. The $As_2S_3$-on-$As_2Se_3$ film #7 was green.

### 2.2 *Photo-Patterning*

Photo-patterning of the film samples was performed using a continuous-wave mode-locked femtosecond laser (Coherent-Mira, 800-nm center wavelength, pulse width $\tau_p = 120$ fs, repetition rate $f = 76$ MHz). The excitation mode was multiphoton absorption because the exposure wavelength was

far from the band edge (530 nm) where linear absorption is negligible.[17,18,31] An acousto-optic modulator (AOM) was used to control film exposure and power in the beam. The laser beam was routed through a beam expander then focused into the film using a $100\times/1.4$ numerical aperture (NA) oil immersion objective (Nikon). The transverse spatial profile of the beam was approximated as a radially symmetric Gaussian having a $1/e^2$ radius of $\omega_0 \approx 175$ nm, and the minor effects of input beam polarization were neglected.[32] The laser beam was focused along the $z$-axis of an arbitrary coordinate system defined so that the substrate lies in the $xy$-plane. The average power $\langle P\rangle$ used to cross-link the films was measured with an integrating sphere at the exit aperture of the objective. The corresponding peak irradiance of the focused beam $I_p$ can be estimated as[33]

$$I_P = \frac{2\langle P\rangle}{f\omega^2\pi\tau}. \tag{1}$$

The film was secured to a sample stage that was translated at a speed of 50 $\mu$m s$^{-1}$ in the $x$-, $y$-, and $z$-axes relative to the laser beam to define the pattern. To create vertical nanoscale pillars, the sample was moved to a given $(x, y)$ coordinate, the AOM was activated, and the sample was translated in the $z$-direction to expose over a vertical length of 2 $\mu$m. This exposure distance was sufficient to bury the beam up to 1 $\mu$m into the substrate and to travel completely through the thickness of the films. To investigate the exposure conditions needed to photo-pattern the films, "dose arrays" were created by fabricating sets of nanopillars over a range of travel speeds and average (avg.) focused laser power that varied from 0.02 to 0.50 mW. Individual arrays consisted of a $9\times 9$ grid of nanopillars separated by a pitch of 500 nm. The term "dose array" will hereafter refer to the entire set of $9\times 9$ grids of nanopillars separated by a pitch of 500 nm and fabricated using laser powers that varied from 0.02 to 0.50 mW.

### 2.3 *Chemical Etching*

One goal for the present effort was to identify etchants and processing conditions that could be used to selectively dissolve unexposed regions of a ChG film, leaving behind material that had been exposed and structurally modified. An "optimal" etchant would yield structures with excellent contrast and feature fidelity limited only by the dimensions of the focused laser spot. Sulfide- and selenide-based ChGs are known to be soluble in basic, polar media.[34] It has been reported that solutions of 0.05 to 5.3 mol. % of diisopentylamine (DIPA) in dimethylsulfoxide (DMSO) can be used to etch thermally deposited $As_2S_3$.[17] Others have reported using solutions of 2 to 3 mol. % DIPA in DMSO.[23,24] In our past work, it was found through visual observation, NMR, and etch-contrast measurements that DIPA is miscible in DMSO only up to circa 1.0 mol. %.[21] A system containing two phases was not expected to etch consistently, and, as a result, all work was performed using 0.5 mol. % DIPA in DMSO, which is well below the miscibility limit.

Etch rates were measured by immersing unexposed films in solutions of 0.5 mol. % DIPA in DMSO and measuring the time required for an etchant to completely dissolve the unexposed ChG film. A video camera was used to record the etch process for the single-layer $As_2S_3$ films (#1 to #6). Because the reflectivity of the $As_2S_3$ layer and the silicon substrate are significantly different, the time at which the etchant reached the $As_2S_3$/Si interface was readily identifiable from changes in the image contrast. For the multilayer $As_2S_3$-on-$As_2Se_3$ film (#7), chemical signatures from the Raman spectra were used to differentiate between the ChG film and the substrate and to determine the time required for the etchant to reach the interface between the two. The etch rate is defined, per the below equation, as the ratio of its thickness to the time required to etch it

$$\text{Etch rate} = \frac{\text{Film thickness}}{\text{Etch duration}}. \tag{2}$$

Films that were photo-patterned via MPL were etched with 0.5 mol. % DIPA in DMSO to reveal the targeted nanostructures. The photo-patterned sample was immersed in the etchant for 60 to 300 s for the $As_2S_3$ films (#1 to #6) and 30 min for the $As_2S_3$-on-$As_2Se_3$ film (#7) and then rinsed with acetone or isopropyl alcohol for 2 min. Scanning electron microscope (SEM) images of the resulting nanostructures were recorded using a Zeiss ULTRA-55 FEG SEM in top-down and profile views. The dimensions of the features ($x$- and $y$-widths) were measured from these images and correlated with film composition, processing conditions, and laser power. The $x$- and $y$-widths are not expected to be exactly the same since a linearly polarized beam focused under a high NA does not produce a rotationally symmetric point spread function.[20,21] This effect is expected to cause the widths to differ by not more than 10%. Rekštytė et al.[35] reported that the observed elongation of polymerized features due to the polarization of the incident laser beam was attributed to heat diffusion and local overheating and was more pronounced for longer wavelengths, higher pulse energies, and longer pulses.

### 2.4 *Spectroscopic and Optical Characterization*

The chemical bonding and structure of $As_2S_3$ films were investigated using micro-Raman spectroscopy[36–39] for samples either in pristine form, immediately following UV or laser exposure, or at various stages of etching. Peaks in the Raman spectra were assigned as described in Refs. 17 and 18. Pristine films were exposed by irradiating samples for 2 min in a Zeta Loctite UV flood chamber equipped with high-pressure mercury lamps that emit broadband UV radiation (65 mW cm$^{-2}$). $As_2S_3$ glasses have absorption coefficients of $10^3$ to $10^4$ cm$^{-1}$ at wavelengths of 380 to 450 nm.[7] The corresponding penetration depth for UV light is 1 to 10 $\mu$m. Given that the penetration depth exceeds the thickness of the films, it can be assumed that the samples were irradiated throughout their full thickness. Pristine films were laser exposed over 100 $\mu$m $\times$ 100 $\mu$m square regions and then etched to create square pads of laser-exposed material that could be studied by Raman spectroscopy. A Horiba Jobin Yvon LabRamHR high-resolution confocal Raman microscope system with an average power of 80 mW at the output and an excitation wavelength of 785 nm was used for measurements taken of the single-layer $As_2S_3$ films (#1 to #6). The laser power was adjusted using an optical density filter to mitigate undesired photo-modifications of the films during measurements. The beam was focused with a 100× microscope objective (NA = 0.9 and WD = 0.21 mm) with a spatial resolution of 2 $\mu$m. The

**Table 2** Film-deposition conditions, the resulting thickness, the observed etch rate, and the widths and shapes of features that were created in the films via MPL at a given minimum average focused power $\langle P \rangle$ and corresponding peak irradiance. Values listed under "thickness" refer to the $As_2S_3$ layer for all films.

| | | | | | Width of smallest features created by MPL at the given laser power/intensity/energy | | | |
|---|---|---|---|---|---|---|---|---|
| Film # | Deposition rate (Å s$^{-1}$) | Thickness of $As_2S_3$ layer (nm) | Unexposed etch rate (nm s$^{-1}$) | Feature shape | $x$-width (nm) | $y$-width (nm) | $\langle P \rangle$ (mW) | Peak irradiance (GW cm$^{-2}$) |
| 1 | 25 | 170 ± 8 | 23.5 ± 6 | Oblate | 204 ± 7 | 226 ± 8 | 0.075 | 4.32 |
| 2 | 25 | 172 ± 9 | 35.2 ± 4 | Oblate | 344 ± 9 | 396 ± 16 | 0.150 | 8.65 |
| 3 | 25 | 166 ± 3 | 39.1 ± 6 | Oblate | 286 ± 12 | 292 ± 9 | 0.100 | 5.76 |
| 4 | 80 | 164 ± 3 | 10.9 ± 1 | Dome | 206 ± 18 | 222 ± 20 | 0.050 | 2.88 |
| 5 | 80 | 159 ± 6 | 2.7 ± 0.1 | Dome | 188 ± 11 | 220 ± 12 | 0.075 | 4.32 |
| 6 | 27 | 1075 ± 0.8 | 19.6 ± 1 | Bead-stacks | 320 ± 16 | 328 ± 29 | 0.175 | 10.1 |
| 7 | 30 | 896 ± 13 | 0.50 ± 0.005 | Cylinder | 120 ± 14 | 125 ± 20 | 0.160 | 9.22 |

backscattered Raman signal was collected and analyzed. For the multilayer $As_2S_3$-on-$As_2Se_3$ film (#7), a Bruker Senterra micro-Raman system with an average power of 10 mW and an excitation wavelength of 785 nm was used. The beam was focused using a 10× microscope objective (NA = 0.3 and WD = 15 mm). The focused beam had a diameter of 50to 200 $\mu$m. An energy-dispersive X-ray spectrometer (Noran system 7) installed on the SEM was used to measure the elemental composition of the films.

Variable-angle spectroscopic ellipsometry (Woollam M2000) was used to measure the dispersion of the refractive index of unexposed, UV-exposed, and laser-exposed films. The probe wavelengths ranged from 600 to 1600 nm. Laser-exposed samples for ellipsometry measurements were created via MPL by rastering the focal point within a 250 $\mu$m × 250 $\mu$m area at an average power just below the damage threshold of the material. Focusing optics were used to collect data from regions as small as 100 $\mu$m × 100 $\mu$m with a spectral resolution of 3 nm at visible wavelengths and 6 nm in the near-IR. A Tauc–Lorentz oscillator method was used to extract the $n$ and $k$ values.[40] The surface roughness and optical bandgap were allowed to vary as free parameters.

## 3 Results and Analysis

### 3.1 *Etch Processing and Composition of Films*

EDX measurements showed that the As-deposited $As_2S_3$ films had an As-to-S atomic ratio of 0.666 ± 0.094, indicating that the thermal deposition process generated samples with the expected stoichiometric elemental composition. Raman spectroscopy was used to study the chemical structure and etch-behavior of As-deposited films. Single-layer $As_2S_3$ films (#1 to #6) and multilayer $As_2S_3$-on-$As_2Se_3$ films (#7) were etched in DIPA/DMSO for varying lengths of time, and Raman spectra were recorded to study chemical species comprising the resulting interface. The features in the spectra were then used to identify chemical signatures in the material (circa 1-$\mu$m Raman sampling depth) and to estimate the time required to remove a given layer entirely. Etch data for all films are presented in Table 2.

The Raman spectra for single-layer $As_2S_3$ films (#6) and multi-layer $As_2S_3$-on-$As_2Se_3$ films (#7) are shown in Figs. 1 and 2. Both exhibit peaks indicative of molecular clusters typically found in thermally deposited $As_2S_3$.[17,18] The peak appearing at 300 cm$^{-1}$ is due to the silicon substrate. The presence of $As_2S_3$ glass is confirmed by the broadbands at 136 and 232 cm$^{-1}$. $As_4S_4$ molecular clusters and As–As homopolar bonds can be assigned to the absorptions at 191, 222, and 363 cm$^{-1}$. The presence of $AsS_3$ pyramidal subunits is confirmed by the peak at 346 cm$^{-1}$. The broad peak at 345 cm$^{-1}$ is assigned to the As–S–As asymmetric stretching mode. S–S homopolar bonds are identified by the peaks around 494 cm$^{-1}$. Features representative of the $As_2Se_3$

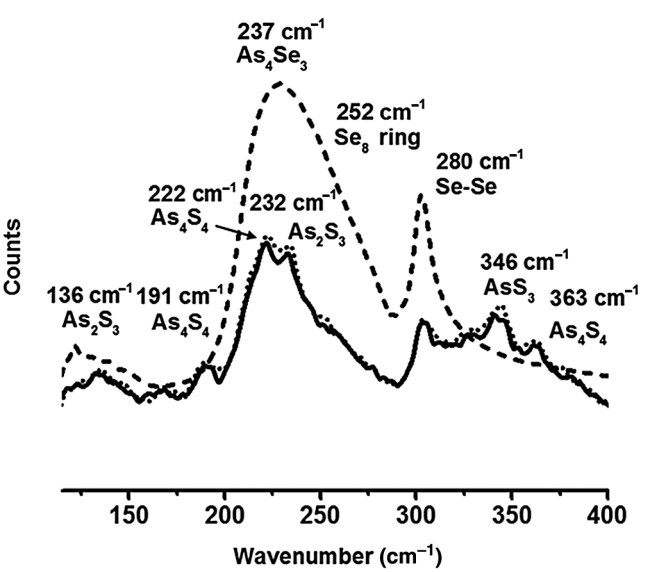


**Fig. 1** Raman spectra of $As_2S_3$-on-$As_2Se_3$ film (#7) in pristine form (solid line) after 5 min of etching (dotted line) and after 30 min of etching (dashed line).

layer include the band for $AsSe_3$ at 227 $cm^{-1}$, $As_4Se_3$ at 237 $cm^{-1}$, Se–Se at 280 $cm^{-1}$, and $Se_8$ rings at 252 $cm^{-1}$.

Films prepared using a high deposition rate (80 Å $s^{-1}$) were found to etch more slowly than those deposited at a low deposition rate (25 to 27 Å $s^{-1}$). The exception to this trend is the $As_2S_3$-on-$As_2Se_3$ film (#7), which is discussed below. The difference in etch speed may result because, under high deposition, a sample can accumulate heat that can cross-link thermally deposited ChG at the substrate interface.[41] However, evidence for this cross-linking is not apparent in the Raman spectra of the films. This is because, compared to the thicker films (#6 and #7), the thin films (#1 to #5) have a shorter Raman interaction path length and reduced signal-to-noise, which makes distinguishing individual peaks from the substrate background signal difficult. Therefore, using Raman spectra to detect differences in cross-linking within the group of thin films (#1 to #5) or between the thin films (#1 to #5) and film (#6) was not possible. Multilayer films were found to etch more slowly than single-layer films that were deposited at similar rates. Figure 1 shows that it takes 30 min to completely remove the 1-$\mu$m-thick layer of $As_2S_3$. In comparison, the $As_2S_3$ films (#1 to #6) etch completely in under 60 s. Figure 2 provides a comparison of the spectra recorded for $As_2S_3$ film (#6), $As_2S_3$-on-$As_2Se_3$ film (#7), and its underlying $As_2Se_3$ layer, which was exposed prior to the Raman measurement by etching away all $As_2S_3$ from an $As_2S_3$-on-$As_2Se_3$ film. The peaks due to As–S species, which would normally appear at 225 $cm^{-1}$, are obscured for the $As_2S_3$-on-$As_2Se_3$ film by a strong, broad peak generated by the underlying $As_2Se_3$ layer. The difference in etch rates may be due to variations in thermal dissipation that occur due to the underlying $As_2Se_3$ layer. For this sample, signals coming from the underlying $As_2Se_3$ layer make it difficult to identify differences in the $As_2S_3$ layer. When thermally depositing films, one must consider unintentional cross-linking that can result from heat accumulated with a high deposition rate, as well as changes in thermal dissipation due to the inclusion of multiple layers. This effect may be mitigated by the use of a temperature-controlled thermal deposition stage.

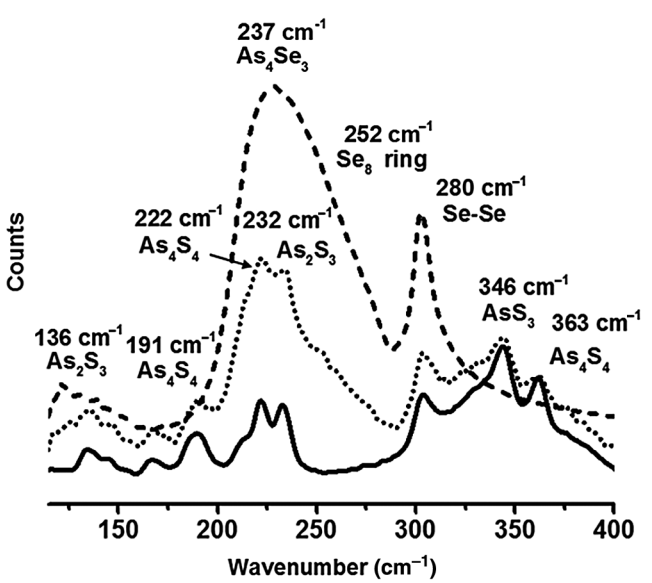


**Fig. 2** Raman spectra of $As_2S_3$ film (#6) in pristine form (solid line), $As_2S_3$-on-$As_2Se_3$ film (#7) in pristine form (dotted line), and the underlying $As_2Se_3$ layer after 30 min of etching (dashed line).

### 3.2 *Multiphoton Lithography in Thermally Deposited $As_2S_3$*

Dose arrays, such as those shown in Fig. 3, were used to study the exposure conditions needed to photo-pattern the films. Samples were exposed over a range of average focused laser powers (corresponding peak irradiance and pulse energy can be found in Table 2) at a fixed scan speed to identify the minimum power needed to create robust features that could survive photo-exposure and subsequent etching. Also measured was the maximum power above which damage or distortion occurs, and how the feature size scales with power between the lower and upper limits. After exposure, the films were removed by etching with 0.5 mol. % DIPA in DMSO. Table 2 presents the measurements of the thickness of the pristine $As_2S_3$ layers, the minimum average laser power needed to photo-pattern robust features, and the sizes of the resulting structures.

The minimum power needed to create robust features was the same within uncertainty for all films, which implies that all films had similar photosensitivity, irrespective of the conditions used to prepare them. The minimum feature sizes that could be obtained varied due to differences in material-substrate adhesion (Table 2). Low power generated small features that were susceptible to delamination during post-exposure etching. $As_2S_3$ films deposited at a high deposition rate (80 Å $s^{-1}$, films #4 and #5) etched more slowly (2.7 nm $s^{-1}$ ± 0.1 nm $s^{-1}$ to 10.9 nm $s^{-1}$ ± 1 nm $s^{-1}$) than those prepared at a low deposition rate (25 Å $s^{-1}$ to 27 Å $s^{-1}$, films #1 to #3 and #6), which etched rapidly (19.6 nm $s^{-1}$ ± 1 nm $s^{-1}$ to 39.1 nm $s^{-1}$ ± 6 nm $s^{-1}$). Dome-shaped features were obtained with films having a low etch rate, presumably because the etchant does not effectively remove cross-linked material closest to the substrate. When features were patterned in fast-etching films, material at the substrate was removed and oblate structures resulted (Fig. 3). Dome-shaped features adhered to the substrate better than oblate features and were more likely to survive postexposure

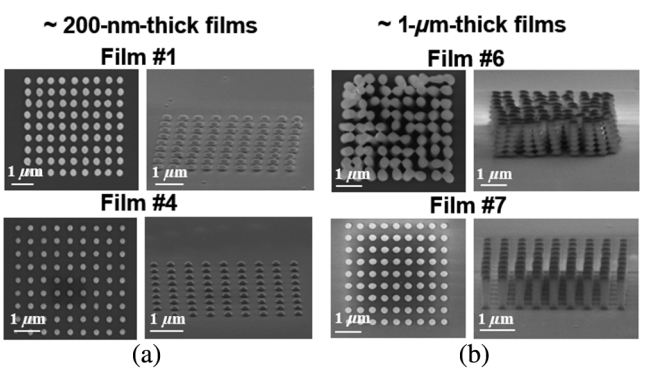


**Fig. 3** (a) Top- and profile-views of nanoscale features fabricated in single-layer ~200-nm-thick $As_2S_3$ films (#1 and #4). The image for $As_2S_3$ film (#1) shows an example of the oblate-shaped features characteristic of laser patterning in films thermally deposited at 25 Å $s^{-1}$. The image for $As_2S_3$ film (#4) shows an example of dome-shaped features characteristic of laser patterning in films thermally deposited at 80 Å $s^{-1}$. (b) Top- and profile-views of nanoscale features fabricated in single-layer ~1-$\mu$m-thick $As_2S_3$ film (#6) and multilayer $As_2S_3$-on-$As_2Se_3$ film (#7) with a ~1-$\mu$m-thick $As_2S_3$ layer, respectively.

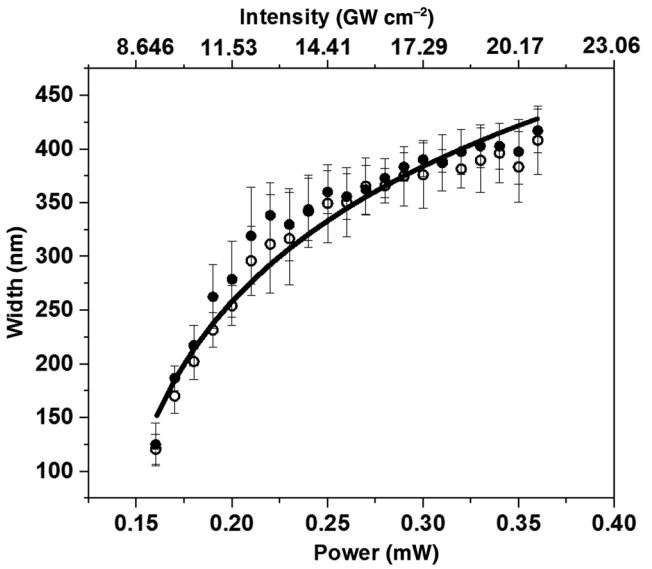


**Fig. 4** Widths of nanofabricated features measured in the *x*- (open circles) and *y*-direction (filled circles) versus average laser power and peak irradiance for structures patterned in an $As_2S_3$-on-$As_2Se_3$ film (#7).

etching, so the smallest feature sizes were obtained with films that yielded dome-shaped structures. Feature formation in the multilayer $As_2S_3$-on-$As_2Se_3$ film (#7) is discussed in Sec. 3.3.

For all films, increasing the laser power produced larger features, consistent with a threshold-related process, such as MPL in photopolymers.[42] Top-view SEM images were used to obtain the widths of structures photo-patterned in the multilayer $As_2S_3$-on-$As_2Se_3$ film (#7) over a range of laser powers and to generate a plot of feature width versus laser power (Fig. 4). The error bars are set at $\pm 1$ standard deviation of the mean. For a threshold-dependent MPL process, the relationship between feature width and the focal-spot width $r_0$, average laser power $\langle P \rangle$, and the threshold-power for producing a feature $\langle P \rangle_{\mathrm{Th}}$ can be described by Eq. (3).[42] The smooth curve in Fig. 4 is a global fit of the feature widths to Eq. (3) with $r_0$ and $\langle P \rangle_{\mathrm{Th}}$ set as free parameters. The good fit suggests that MPL in thermally deposited $As_2S_3$ forms features via a threshold-dependent photocuring process[42]

$$\text{Feature width} = \sqrt{2} r_0 \sqrt{\ln \frac{\langle P \rangle}{\langle P \rangle_{\mathrm{Th}}}}. \tag{3}$$

### 3.3 *Standing-Wave Interference and Nanostructure Morphology*

MPL was performed by scanning the focal point through the film along a path perpendicular to the substrate. To first approximation, this should produce nearly cylindrical nanostructures with a height determined by the thickness of the film. Yet oblate ellipsoids (Fig. 3) were obtained from MPL in ~165-nm-thick single-layer films prepared at low deposition rates (films #1 to #3). And MPL in a 1-$\mu$m-thick single-layer film (#6) produced stacks of oblate ellipsoids or nanobeads. These observations can be explained by considering how light reflected at the interface modulates the exposure in the photoactive $As_2S_3$ layer of a given film.

Reflection at the silicon substrate of a single-layer film produces a standing wave that modulates the film exposure with distance from the substrate. Interference due to backreflected light is well known in conventional photolithography[43] and has also been reported for MPL of polymeric lines on a gold-coated substrate.[35] The interference maxima are separated by distance $d_{\mathrm{max}}$ given by

$$d_{\mathrm{max}} = \frac{\lambda}{2 n_{\mathrm{film}}}, \tag{4}$$

where $\lambda$ is the wavelength of the excitation beam and $n$ is the index of refraction of the film. At $\lambda = 800$ nm, the refractive index of the $As_2S_3$ film and the silicon substrate are $n_{\mathrm{film}} = 2.5$ and $n_{\mathrm{Si}} = 3.5$, respectively, and $d_{\mathrm{max}} = 160$ nm. The ratio of the amplitudes of the reflected and incident field will then be $(n_{\mathrm{Si}} - n_{\mathrm{film}})/(n_{\mathrm{Si}} + n_{\mathrm{film}}) = 0.17$, resulting in large exposure modulation. Because $n_{\mathrm{film}} < n_{\mathrm{Si}}$, the reflected wave is antiphase with the incident beam, leading to destructive interference at the interface and constructive interference at distances $(m + 1/2) d_{\mathrm{max}}$ from the interface, where $m$ is a whole number that counts the interference maxima. Destructive interference at the interface results in significant underexposure immediately at the substrate and at multiples of $d_{\mathrm{max}}$ from the interface, producing periodic oblate-shaped structures in the thick film or a single oblate structure in thin films, which have thicknesses very close to $d_{\mathrm{max}}$. The predicted form for the nanostructures described here is consistent with those observed experimentally.

According to Eq. (4), the center-to-center distance between nanobeads in a stack and the number of beads formed within a given film should depend on the wavelength of the excitation beam. To confirm the effects of standing-wave interference, MPL was performed in the single layer, 1-$\mu$m-thick film (#6) at $\lambda = 720$, 800, and 900 nm. The results are shown in Fig. 5. As the excitation wavelength increases from 720 to 800 nm and then to 900 nm, the center-to-center distance between beads increases from 140 nm $\pm$ 5 nm to 171 nm $\pm$ 3 nm and finally to 198 nm $\pm$ 5 nm. Correspondingly, the number of beads within the stacks decreases with excitation wavelength from 8 to 7 to 6. Figure 5 shows the observed distance between beads versus $\lambda$, as well as that predicted using Eq. (4). For this calculation, the values for the index of refraction were obtained by ellipsometry (discussed below) and were taken as $n = 2.56$, 2.50, and 2.48, for $\lambda = 720$, 800, and 900 nm, respectively. The measured and predicted bead separations are in good agreement. These results confirm that the form of the nanostructures created by MPL in single layer, 1-$\mu$m-thick films are strongly affected by standing-wave interference.

AR coatings can be created [Fig. 6(a)] by adding a layer of material that has a thickness of $m\lambda/4n$, where $m = 1, 3, 5, \ldots$, and the refractive index $n$ is intermediate between those of the original interface. The thickness of the AR layer is chosen so that the waves reflected at the two interfaces recombine, shifting in phase by 180 deg. This leads to destructive interference that cancels the reflection and eliminates modulation of the irradiance near the substrate.

For the present work, $As_2Se_3$ was selected as the AR material because it can be thermally deposited and it has

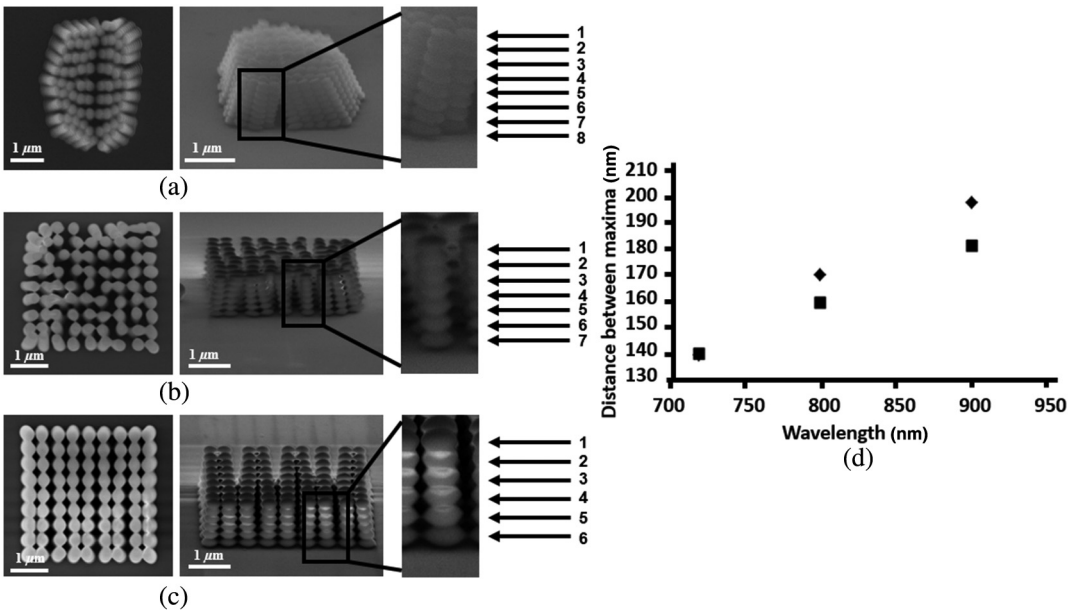


**Fig. 5** Top- and profile-view SEM images of nanobeads fabricated in the 1-$\mu$m-thick single-layer $As_2S_3$ film (#6) at fabrication wavelengths of (a) 720, (b) 800, and (c) 900 nm. The scale bar corresponds to 1 $\mu$m. The third column gives magnified images of the nanobeads and the number of beads seen in each stack for each fabrication wavelength. (d) Plot of the measured (filled diamond) and expected (filled square) center-to-center spacing of the beads within a stack as a function of fabrication wavelength.

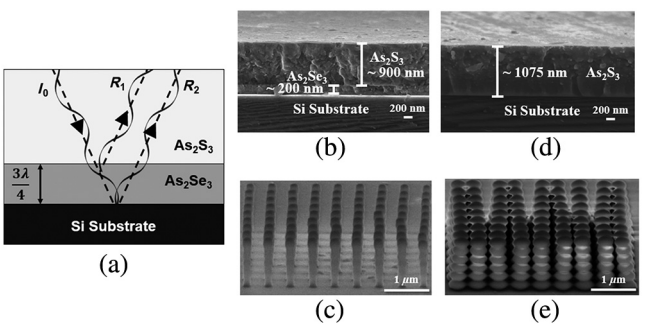


**Fig. 6** (a) Schematic image of the interference resulting from an interface bearing a three-quarter-wave AR coating of thermally deposited $As_2Se_3$. (b) Profile-view SEM image of a cleaved multilayer $As_2S_3$-on-$As_2Se_3$ film (#7) and (c) side-view SEM image of nanostructures fabricated by MPL in this film. (d) Profile-view SEM image of a cleaved 1-$\mu$m-thick single-layer $As_2S_3$ film (#6) and (e) side-view SEM image of nanostructures fabricated by MPL in this film.

$n \sim 3.0$ at 800 nm, which is an intermediate between the values of $n$ for the silicon substrate and the $As_2S_3$ layer. AR-coated multilayer films [#7, Fig. 6(b)] were formed by thermally depositing $As_2Se_3$ to a thickness of 200 nm directly onto the silicon substrate and then depositing a layer of photo-patternable $As_2S_3$ atop the AR layer. The thickness of the $As_2Se_3$ was chosen so that it would serve as a $3/4\lambda$ AR-layer ($m = 3$). Nanofeatures were then patterned in the multilayer films as described in Sec. 2.2.

Figures 6(c) and 6(e) show side-view SEM images of the nanofeatures created by MPL in the multilayer film and in the 1-$\mu$m-thick single-layer film, respectively. Features patterned in the multilayer $As_2S_3$-on-$As_2Se_3$ film (#7) were cylindrical in shape and show little evidence of the modulated irradiance that forms the nanobeads. These data prove that the addition of the $As_2Se_3$ AR layer significantly reduces the standing wave interference. Although the $As_2S_3$ in both films should have similar photosensitivity, larger powers were required to produce features of similar dimensions in the $As_2S_3$-on-$As_2Se_3$ film (#7). For example, features with widths of ~320 nm were formed at an average power of 0.175 mW in the single-layer films, whereas an average power of 0.230 mW was needed to produce similarly sized features in the multilayer film (see also Table 2 and Fig. 4). This can be understood because light reflecting from the surface of the single-layer films increases the effective irradiance near the substrate, so lower overall power is needed to create features.

Surface tension during etch processing and drying results in the collapse of the photo-patterned structures and overall deformation of the array (Fig. 5).[44] Relative to the stacks of nanobeads, the cylinder-shaped features have increased material-substrate adhesion, so delamination due to capillary forces is reduced and smaller-sized features can be obtained. The smallest features obtained with the $As_2S_3$-on-$As_2Se_3$ film (#7) had minimum widths of 120 nm $\pm$ 14 nm, whereas the smallest size that could be obtained for the $As_2S_3$ film (#6) had minimal widths of 320 nm $\pm$ 16 nm. Overall, these experiments show that AR-layers can be used to control or suppress standing wave interference, which affords greater control over the shapes and sizes of features that can be produced by MPL in thermally deposited $As_2S_3$.

### 3.4 *Micro-Raman Characterization of Unexposed and Photo-Exposed Films*

Micro-Raman spectroscopy was used to investigate the chemical bonding of pristine single- and multilayer $As_2S_3$ films and to study how UV and laser exposure alter the chemical structure and resulting optical properties. Resonances in the spectra were assigned as described in Sec. 3.1 and Refs. 17, 18, and 45. Wong et al.[17] and Zoubir

et al.[18] reported that thermally deposited films are more photosensitive when they contain molecular clusters, such as $As_4S_6$, $As_4S_4$, and $S_8$, that include homopolar bonds (e.g., As–As and S–S). These bonding arrangements also cause the films to have lower density, index of refraction, and film photostability than that seen in the parent bulk $As_2S_3$.[27] All pristine single-layer $As_2S_3$ films (#1 to #6) and multilayer $As_2S_3$-on-$As_2Se_3$ films (#7) displayed similar low-frequency peaks at 190 and 222 $cm^{-1}$, indicating the presence of $As_4S_4$ molecular clusters and As–As homopolar bonds.[46–48] Deposition rates ranging from 25 to 80 Å $s^{-1}$ produced films of similar composition and photosensitivity. The film deposition rates, thickness, and observed etch rates (Table 2) could not be unambiguously correlated with the photosensitivity or chemical bonding.

Thick-layer films (#6 and #7) were used to study how UV and laser exposure affect the chemical structure of thermally deposited $As_2S_3$ because they offered a longer Raman interaction path length and better signal-to-noise than thin-layer films. Figure 7 shows how the single-layer $As_2S_3$ film behaves under UV and laser exposure. UV exposure breaks the homopolar bonds assignable to $As_4S_4$ clusters (191 and 222 $cm^{-1}$) with concomitant formation of heteropolar bonds associated with $As_2S_3$ structural units (232 $cm^{-1}$). The decrease in homopolar $As_4S_4$ bonds and the formation of heteropolar $As_2S_3$ bonds indicate that the thermally deposited material fragments photochemically and then cross-links reforming the $As_2S_3$ bulk-glass network.[18] Figure 8 shows that similar photochemistry occurs for $As_2S_3$-on-$As_2Se_3$ films (#7). With both UV and laser exposure, peaks due to homopolar $As_4S_4$ bonds diminish (191 $cm^{-1}$), whereas the resonances assignable to heteropolar $AsS_3$ units (346 $cm^{-1}$) increase. Relative to single-layer films, the $As_2S_3$-on-$As_2Se_3$ films give much more complex spectra because they include resonances due to As–Se species in the AR coating. For both the single- and multilayer films, the photochemical cross-linking of the $As_2S_3$ glass films appears to be more thorough under laser excitation, as little signal remains from homopolar bonds following laser patterning. Overall, the Raman data show that both UV

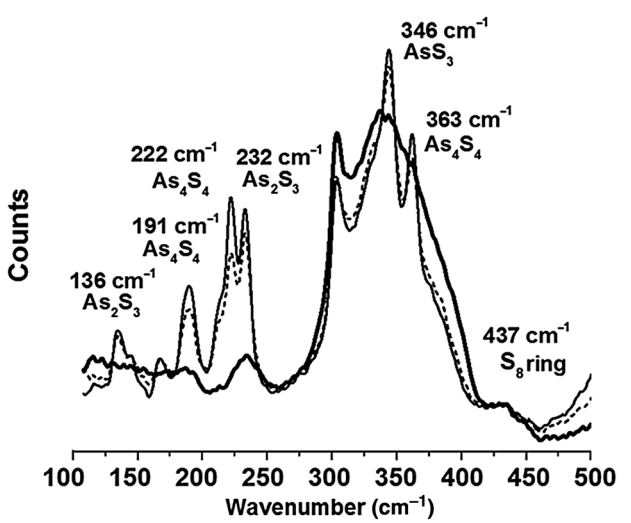


**Fig. 7** Raman spectra of single-layer $As_2S_3$ films (#6) in pristine form (thin solid line), after UV-exposure (dashed line), and after laser exposure (thick solid line).

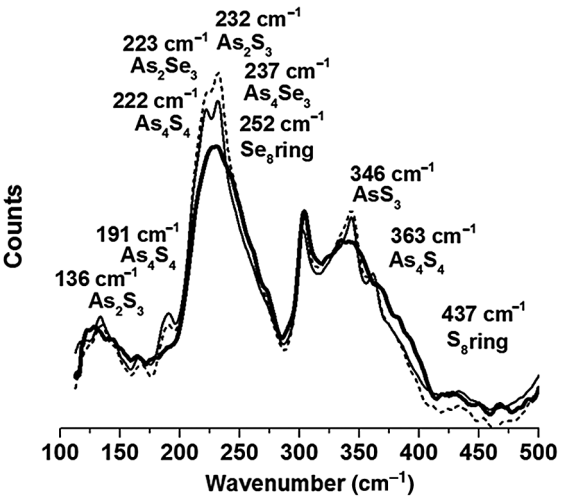


**Fig. 8** Raman spectra of multilayer $As_2S_3$-on-$As_2Se_3$ films (#7) in pristine form (thin solid line), after UV exposure (dashed line), and after laser exposure (thick solid line).

excitation and laser excitation can be used to photochemically cross-link thermally deposited $As_2S_3$ films back to an $As_2S_3$ bulk-glass network solid, even when an underlying AR-layer of $As_2Se_3$ is present.

The findings reported here are consistent with previous studies of the photosensitive, thermally deposited $As_2S_3$ films.[18] Zoubir et al.[18] studied Raman measurements from laser exposed thermally deposited single-layer $As_2S_3$ films and showed that laser exposure of $As_2S_3$ films resulted in a decrease of low-frequency homopolar bonds as more $As_4S_4$ molecular clusters reorganized to form the glass network. This was similar to the decrease seen in both the single-layer $As_2S_3$ film (#6) and the multilayer $As_2S_3$-on-$As_2Se_3$ film (#7).

### 3.5 *Index of Refraction for Unexposed and Photo-Exposed Films*

The index of refraction $n$ (Fig. 9) and extinction coefficient $k$ were obtained from spectroscopic ellipsometry measurements performed on unexposed, UV-exposed, and laser-exposed single-layer $As_2S_3$ films (#6) and multilayer $As_2S_3$-on-$As_2Se_3$ films (#7). The extinction coefficient $k$ (not shown) was effectively zero for all films over the 600- to 1600-nm wavelength range, and it did not change significantly when the films were exposed to UV or laser light. The index of refraction for pristine single-layer $As_2S_3$ was 0.05 units greater than that of the multilayer films, and both exhibited similar dispersion across the range of wavelengths measured. The difference in refractive index between the two samples is most likely due to the difference in the conditions used to deposit the films.

The index of refraction was found to increase with the degree of photo-exposure and was consistent with the increase in polarizability that results upon cross-linking to the network solid (Fig. 9).[36,37,49,50] UV exposure increased the index of refraction by circa 0.05 units for the single-layer $As_2S_3$ film and 0.02 units for the $As_2S_3$-on-$As_2Se_3$ film. Laser exposure increased the index of refraction by a greater degree, reaching 0.09 units for the single-layer film and 0.08 units for the multilayer film. This implies

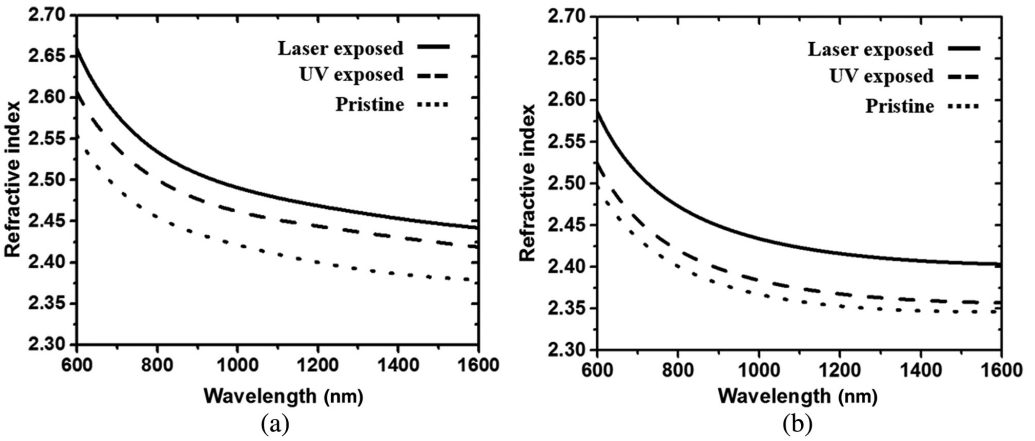


**Fig. 9** Values of the index of refraction $n$ obtained from spectroscopic ellipsometry measurements of single-layer $As_2S_3$ films (#6) and multilayer $As_2S_3$-on-$As_2Se_3$ films (#7). (a) Index of refraction for single-layer $As_2S_3$ films (#6) in pristine form, after UV exposure, and after laser exposure. (b) Index of refraction for multilayer $As_2S_3$-on-$As_2Se_3$ films (#7) in pristine form, after UV exposure, and after laser exposure.

that the laser exposure produced a higher degree of cross-linking throughout the depth of the film, which is consistent with molecular fragments reorganizing to form a network solid, as observed from the Raman spectra of photo-exposed films.[25]

The changes in the index of refraction described above are also consistent with earlier reports of photo-exposed, thermally deposited $As_2S_3$ films.[27] Dispersion curves found in the literature extend over probe wavelengths of 500 to 2000 nm and have similar form to those reported here, but slightly lower values overall.[51]

### 3.6 *Optical Function of Nanostructure Arrays*

Two-dimensional (2-D) diffraction gratings were fabricated by MPL in the $As_2S_3$ films to explore how the exposure and etch protocols could be used to create optically functional devices. Figure 10 shows SEM images of the fabricated pad. A 250 $\mu$m × 250 $\mu$m array of nanopillars was photopatterned in a multilayer $As_2S_3$-on-$As_2Se_3$ film (#7). The pillars were positioned on a square grid with a pitch of 500 nm. An average focused laser power of 0.18 mW was used, generating pillars with an average width of 210 nm ± 15 nm. The height of the pillars was fixed by the thickness of the film and found to be 907 nm ± 10 nm. The nanopillar arrays were robust and homogenous throughout the array. The arrays were optically characterized as 2-D gratings by illuminating them with white light (Fig. 11) or the output of an HeNe laser at $\lambda = 633$ nm (Fig. 12) and then imaging and spectrally analyzing the resulting diffraction patterns.

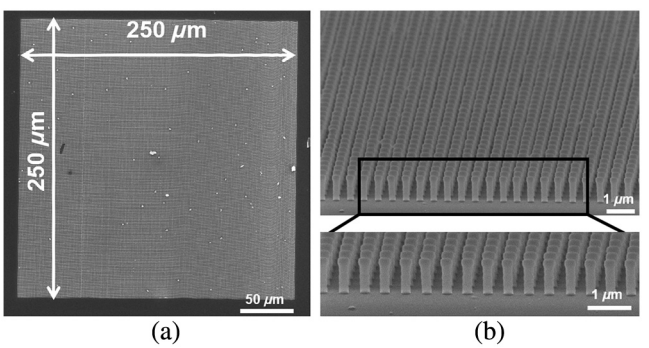


**Fig. 10** (a) Top-down and (b) side-view SEM images of a 250 $\mu$m × 250 $\mu$m nanostructured pillar array fabricated by MPL in an $As_2S_3$-on-$As_2Se_3$ film (#7). The pillars are separated by a pitch of 500 nm.

Figure 11 shows the diffraction observed when a device was illuminated with white light incident at an angle of 60 deg measured normal to the sample surface. The device uniformly diffracted white light and appeared opalescent [Fig. 11(a)]. Nonuniformities in the array were observed as a decrease in diffraction intensity along the top edge of the structure. The wavelength of the diffracted light was measured with a spectrophotometer as a function of incidence angle [Fig. 11(b)]. The device produced spectrally sharp diffraction across the entire range of visible wavelengths. The center wavelength of the diffraction band increased monotonically with the angle of incidence.

Figure 12 shows the diffraction observed when the device was illuminated with the unfocused output of a HeNe laser at $\lambda = 633$ nm. In addition to a reflected beam, multiple diffracted orders were observed. The geometry of the incident, reflected, and diffracted beams is shown schematically in Fig. 12(c). The angles of the incident and diffracted beams were measured and found to be in good agreement with those predicted by the diffraction equation

$$\sin\theta_i + \sin\theta_d = \frac{m\lambda}{d}, \tag{5}$$

where $m$ is the order of the diffracted beam, $\lambda$ is the wavelength of the light in vacuum, $d$ is the grating period, $\theta_i$ is the angle between the incident light and the grating normal, and $\theta_d$ is the angle between the diffracted order and the grating normal. Each diffracted order consisted of a small-angle, fourfold symmetric diffraction pattern, visible in Fig. 12(d). Because the nanopillar array is square and finite in size, it behaves like a limiting aperture that further diffracts each beam into the fourfold symmetric pattern that was observed.

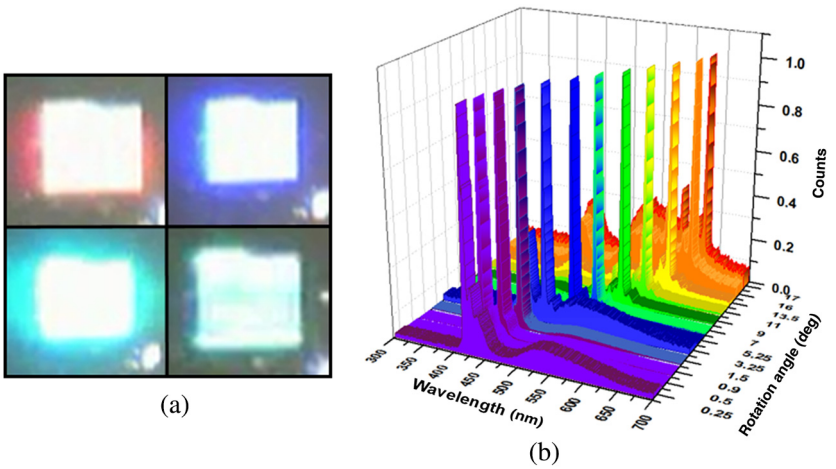


**Fig. 11** (a) Optical images of the 250 $\mu$m × 250 $\mu$m nanostructured pillar array showing that the structure diffracts light of different colors as the angle of incidence is changed. (b) Plot of the diffracted light intensity versus wavelength for white light incident at varying angles.

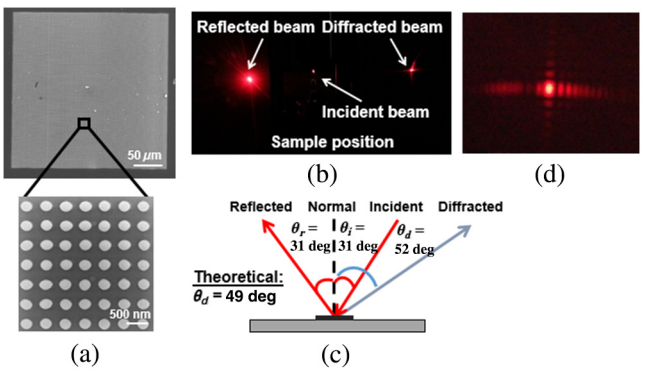


**Fig. 12** (a) Top-down SEM image of the 250 $\mu$m × 250 $\mu$m nanostructured pillar array in film #6 with a close-up image showing the tops of individual structures. (b) Optical image of the incident, reflected, and diffracted beams. (c) Diagram depicting the actual angle for the reflected and diffracted beams and the predicted angle for the diffracted beam. (d) Close-up optical image of the actual refracted beam pattern.

## 4 Conclusions

This work reports a detailed study of the processing of thermally deposited $As_2S_3$ for MPL. The composition of the films and the deposition rates used to prepare them were correlated with the chemical structure, etch processibility, and photosensitivity of the material, as well as how these factors affect the morphology of nanostructures that can be created by MPL in $As_2S_3$. The investigation included thin and thick single-layer films of $As_2S_3$ deposited onto silicon substrates. It also included multilayer films in which $As_2Se_3$ was deposited between the substrate and the $As_2S_3$ layer to suppress standing wave interference that modifies the form of photo-patterned nanostructures.

The rate of thermal deposition was found to strongly affect the etch-resistance of the material but not the photosensitivity. Photo-patterning chemically cross-links the thermally deposited $As_2S_3$ back to a network solid, which is accompanied by an increase in the index of refraction. The sizes of nanopatterned features were observed to increase with the average focused laser power, suggesting that the photo-curing proceeds via a threshold-dependent process, much like an organic photoresist. Laser exposure in the single-layer $As_2S_3$ films without an AR coating produced oblate structures, dome-shaped structures, or stacks of nanobeads, depending upon the film thickness. Using the knowledge gained from this investigation, one could in principle pattern ellipsoidal nanoparticles or stacks of multiple nanoparticles with precise control over their size, shape, and composition. These nanoparticles could then be regioselectivity positioned on a surface relative to active features or components. This could be used to create a wide range of devices, including detectors, sensors, and sensor arrays. Laser exposure in the multilayer $As_2S_3$-on-$As_2S_3$ film produced features that were cylindrical in shape, indicating that the AR layer is effective in eliminating the standing wave effect. Cylindrical features had increased material-substrate adhesion and were therefore more likely to obtain a smaller size (~120 nm) than bead-shaped features (~320 nm) before delamination. Processing conditions were developed for producing large, homogeneous nanostructure arrays with diffractive optical function.

Knowledge of the photo- and etch-processing of ChG films resulting from this work will help further the use of MPL in ChGs to create high-performance photonics devices and IR optics. For example, meta-optics can be designed to function over a specified wavelength range through control of subwavelength features.[52] By patterning features in materials systems, such as ChGs, meta-optics can be developed with expanded optical, mechanical, and thermal-optical properties for wider applications.

### *Acknowledgments*

This work was partially supported by the NSF CAREER award DMR/CHE-0748712 and DMR-1337758; Lockheed Martin; the Florida High-Tech Corridor Council; the Space Research Initiative Program, through the Florida Space Institute, hosted at the University of Central Florida; and the National Aeronautics and Space Administration, through the University of Central Florida's NASA-Florida Space Grant Consortium. Anna Lewis, Gerald Richardson, and Shreya Labh were supported by UCF SURF scholarships. The authors thank Dr. Pieter Kik and Mr. Chatdanai Lumdee for assistance with the ellipsometry measurements and the referees for their thoughtful and constructive comments.

## References


1. C. Tsay et al., "Mid-infrared characterization of solution-processed $As_2S_3$ chalcogenide glass waveguides," *Opt. Express* **18**, 15523–15530 (2010).
2. A. Rodensa et al., "Three-dimensional mid-infrared photonic circuits in chalcogenide glass," *Opt. Lett.* **37**, 392–394 (2012).
3. X. H. Zhang, Y. Guimond, and Y. Bellec, "Production of complex chalcogenide glass optics by molding for thermal imaging," *J. Non-Cryst. Solids* **326**, 519–523 (2003).
4. D. H. Cha et al., "Effect of temperature on the molding of chalcogenide glass lenses for infrared imaging applications," *Appl. Opt.* **49**, 1607–1613 (2010).
5. D. H. Cha et al., "Fabrication of molded chalcogenide-glass lens for thermal imaging applications," *Appl. Opt.* **51**, 5649–5656 (2012).
6. K. J. Ma et al., "Contactless molding of arrayed chalcogenide glass lenses," *J. Non-Cryst. Solids* **357**, 2484–2488 (2011).
7. A. Zakery and S. R. Elliot, "An introduction to chalcogenide glasses," in *Optical Nonlinearities in Chalcogenide Glasses and Their Applications*, W. T. Rhodes, Ed., Vol. **135**, pp. 1–28, Springer, New York (2007).
8. J. D. Musgraves, S. Danto, and K. Richardson, "Thermal properties of chalcogenide glasses," in *Chalcogenide Glasses: Preparation, Properties and Applications*, J.-L. Adam and X. Zhang, Eds., pp. 82–112, Woodhead Publishing, Cambridge (2014).
9. D. W. Hewak et al., "Chalcogenide glasses for photonics device applications," in *Photonic Glasses and Glass Ceramics*, G. S. Murugan, Ed., pp. 92–102, Research Signpost, Kerala, India (2010).
10. J. D. Musgraves et al., "Chalcogenide glass thin-film and fiber structures for chemical and biological sensing," in *Amorphous Chalcogenides: Advances and Applications*, R. Wang, Ed., pp. 203–250, CRC Press, Boca Raton, Florida (2014).
11. J. W. Hutchinson, *Stresses and Failure Modes in Thin Films and Multilayers*, Technical University of Denmark, Lyngby, Kongens Lyngby, Denmark (1996).
12. G. Curatu, "Design and fabrication of low-cost thermal imaging optics using precision chalcogenide glass molding," *Proc. SPIE* **7060**, 706008 (2008).
13. R. J. Benjamin, "Diamond turning at a large optical manufacturer," *Opt. Eng.* **17**, 574–577 (1978).
14. Y. Zha and C. B. Arnold, "Solution-processing of thick chalcogenide and metal-chalcogenide structures by spin-coating and multilayer lamination," *Opt. Mater. Express* **3**, 309–317 (2013).
15. Y. Zha, M. Waldmann, and C. B. Arnold, "A review on solution processing of chalcogenide glasses for optical components," *Opt. Mater. Express* **3**, 1259–1272 (2013).
16. D.-Y. Choi et al., "Photo-induced and thermal annealing of chalcogenide films for waveguide fabrication," *Phys. Procedia* **48**, 196–205 (2013).
17. S. Wong et al., "Direct laser writing of three-dimensional photonic crystals with a complete photonic bandgap in chalcogenide glasses," *Adv. Mater.* **18**, 265–269 (2006).
18. A. Zoubir et al., "Direct femtosecond laser writing of waveguides in $As_2S_3$ thin films," *Opt. Lett.* **29**, 748–750 (2004).
19. C. M. Schwarz et al., "Fabrication and characterization of micro-structures created by direct laser writing in multi-layered chalcogenide glass," *Proc. SPIE* **9374**, 937403 (2015).
20. C. M. Schwarz et al., "Multi-photon lithography of 3D micro-structures in $As_2S_3$ and $Ge_5(As_2Se_3)_{95}$ chalcogenide glasses," *Proc. SPIE* **9759**, 975916 (2016).
21. C. M. Schwarz et al., "Processing and properties of arsenic trisulfide chalcogenide glasses for direct laser writing of 3D micro-structures," *Proc. SPIE* **8974**, 89740P (2014).
22. K. A. Cerqua-Richardson et al., "Comparison of nonlinear optical properties of sulfide glasses in bulk and thin film form," *Opt. Mater.* **10**, 155–159 (1998).
23. E. Nicoletti et al., "Observation of multiple higher-order stopgaps from three-dimensional chalcogenide glass photonic crystals," *Opt. Lett.* **33**, 2311–2313 (2008).
24. E. Nicoletti et al., "Wide-angle stop-gap chalcogenide photonic crystals generated by direct multiple-line laser writing," *Appl. Phys. B* **105**, 847–850 (2011).
25. T. V. Galstian et al., "Photo-induced self-developing relief gratings in thin film chalcogenide $As_2S_3$ glasses," *J. Lightwave Technol.* **15**, 1343–1347 (1997).
26. E. Nicoletti et al., "Generation of $\lambda/12$ nanowires in chalcogenide glasses," *Nano. Lett.* **11**, 4218–4221 (2011).
27. D. Choi et al., "Thermal annealing of arsenic tri-sulphide thin film and its influence on device performance," *J. Appl. Phys.* **107**, 053106 (2010).
28. A. Saliminia et al., "Temperature dependence of Bragg reflectors in chalcogenide $As_2S_3$ glass slab waveguides," *J. Opt. Soc. B* **17**, 1343–1348 (2000).
29. J.-F. Viens et al., "Fabrication and characterization of integrated optical waveguides in arsenic (S, Se)-based chalcogenide glasses," *J. Lightwave Technol.* **17**, 1184–1191 (1999).
30. B. Gleason, "Designing optical properties in infrared glass," Doctor of Philosophy, Clemson University, Clemson (2015).
31. A. Abd-El Mongy, "Photoinduced changes in $As_2S_3$ thin films," *Egypt. J. Solids* **29**, 261–272 (2006).
32. H.-B. Sun et al., "Experimental investigation of single voxels for laser nanofabrication via two-photon photopolymerization," *Appl. Phys. Lett.* **83**, 819–821 (2003).
33. L. Jonušauskas et al., "Optically clear and resilient free-form $\mu$-optics 3D-printed via ultrafast laser lithography," *Materials* **10**, 12 (2017).
34. Y. Zha, M. Waldmann, and C. B. Arnold, "A review on solution processing of chalcogenide glasses for optical components," *Opt. Mater. Express* **3**, 1259–1272 (2013).
35. S. Rekštytė, T. Jonavičius, and M. Malinauskas, "Direct laser writing of microstructures on optically opaque and reflective surfaces," *Opt. Lasers Eng.* **53**, 90–97 (2014).
36. J. D. Musgraves, K. Richardson, and H. Jain, "Laser-induced structural modification, its mechanisms, and applications in glassy optical materials," *Opt. Mater. Express* **1**, 921–935 (2011).
37. T. Anderson et al., "Femtosecond laser photo-response of $Ge_{23}Sb_7S_{70}$ films," *Opt. Express* **16**, 20081–20098 (2008).
38. A. Zoubir et al., "Laser-induced defects in fused silica by femtosecond IR irradiation," *Phys. Rev. B* **73**, 224117 (2006).
39. W. Li et al, "Role of S/Se ratio in chemical bonding of As-S-Se glasses investigated by Raman, XPS and EXAFS spectroscopies," *J. Appl. Phys.* **98**, 493–503 (2005).
40. R. A. Synowicki and T. E. Tiwald, "Optical properties of bulk c-$ZrO_2$, c-MgO and a-$As_2S_3$ determined by variable angle spectroscopic ellipsometry," *Thin Film Solids* **455–456**, 248–255 (2004).
41. S. M. Kuebler and K. A. Richardson, personal communication (2014).
42. H. E. Williams, "Photophysical and photochemical factors affecting multi-photon direct laser writing using the cross-linkable epoxide SU-8," Doctor of Philosophy, University of Central Florida, Orlando, Florida (2013).
43. C. A. Mack, *Fundamental Principles of Optical Lithography: The Science of Microfabrication*, Wiley, Hoboken, New Jersey (2007).
44. S. Maruo, T. Hasegawa, and N. Yoshimura, "Single-anchor support and supercritical $CO_2$ drying enable high-precision microfabrication of three-dimensional structures," *Opt. Express* **17**, 20945–20951 (2009).
45. M. S. Iovu et al., "Raman spectra of $As_xSe_{100-x}$ and $As_{40}Se_{60}$ glasses doped with metals," *Chalcogenide Lett.* **2**, 21–25 (2005).
46. K. Richardson et al., "Engineering glassy chalcogenide materials for integrated optics applications," in *Photo-Induced Metastability in Amorphous Semiconductors*, A. V. Kolobov, Ed., pp. 383–402, Wiley-VCH, Morlenbach, Germany (2007).
47. H. Y. Yuen, "Inscription and characterization of fiber Bragg gratings in multi-mode $As_2S_3$ optical fiber at 1550 nm using interferometric and phase mask methods," Doctor of Philosophy, Iowa State University, Ames, Iowa (2006).
48. A. Kovalskiy et al., "Chalcogenide glass thin film resists for grayscale lithography," *Proc. SPIE* **7273**, 72734A (2009).
49. N. Carlie et al., "Measurement of the refractive index dispersion of $As_2Se_3$ bulk glass and thin films prior to and after laser irradiation and annealing using prism coupling in the near- and mid-infrared spectral range," *Rev. Sci. Instrum.* **82**, 053103 (2011).
50. L. Petit et al., "Comparison of the photo-response of chalcogenide glasses to IR fs laser exposure used for micro-structuring," *IEEE J. Sel. Top. Quantum Electron.* **14**, 1323–1334 (2008).
51. K. Petkov, "Compositional dependence of the photoinduced phenomena in thin film chalcogenide films," *J. Optoelectron. Adv. Mater.* **4**, 611–629 (2002).
52. M. Khorasaninejad et al., "Metalenses at visible wavelengths: diffraction-limited focusing and subwavelength resolution imaging," *Science* **352**, 1190–1194 (2016).



**Casey M. Schwarz** completed her PhD in physics at the University of Central Florida (UCF) in 2012 studying the effects of radiation on semiconductor transport properties using electron beam induced current and cathodoluminescence techniques under the supervision of professor Leonid Chernyak. Then she joined the Kuebler Group as postdoctoral scholar investigating the processing and properties of novel materials for optical applications. She joined Ursinus College as an assistant professor of physics in 2016.

**Stephen M. Kuebler** earned his DPhil in chemistry at the University of Oxford and his BS in chemistry and BA in German at Tulane University. He completed postdoctoral research at CalTech and the University of Arizona. Currently, he is an associate professor of chemistry and optics at the University of Central Florida. His research interests include nonlinear optical materials and photochemistry and using 3D nano- and microfabrication to create functional nanophotonic devices.

Biographies for the other authors are not available.